

PAPER

First-principles Raman spectra of MoS₂, WS₂ and their heterostructures†Cite this: *Nanoscale*, 2014, 6, 5394

Liangbo Liang and Vincent Meunier*

Received 30th December 2013
Accepted 11th February 2014

DOI: 10.1039/c3nr06906k

www.rsc.org/nanoscale

Raman spectra of MoS₂, WS₂, and their heterostructures are studied by density functional theory. We quantitatively reproduce existing experimental data and present evidence that the apparent discrepancy between intensity ratios observed experimentally can be explained by the high sensitivity of the Raman-active modes to laser polarization. Furthermore, MoS₂/WS₂ heterostructures up to four layers are considered in every possible combination and stacking order. Each heterostructure configuration possesses a unique Raman spectrum in both frequency and intensity that can be explained by changes in dielectric screening and interlayer interaction. The results establish a set of guidelines for the practical experimental identification of heterostructure configurations.

1 Introduction

Transition metal dichalcogenides MX₂ (M = Mo, W; X = S) are layered structures stacked by weak van der Waals (vdW) forces, where one X–M–X layer is a covalently bonded hexagonal quasi-2D network.^{1,2} Recently, similar to graphene, atomically thin MoS₂ layers have been successfully obtained using the exfoliation method.³ Field-effect transistors based on monolayer MoS₂ have shown a room-temperature electron mobility close to that of graphene nanoribbons and a current on/off ratio up to 10⁸.⁴ Bulk MoS₂ is an attractive semiconducting material for photovoltaic and photocatalytic applications.⁵ Furthermore, from the bulk phase to single-layer phase, a transition from indirect to direct electronic band gap occurs in MoS₂, together with an enhancement of photoluminescence (PL).^{6,7} Similarly, single-layer WS₂ triangular islands have been recently synthesized and found to show intense room-temperature PL associated with specific edges.⁸ These superior optical and electronic properties make ultrathin MoS₂ and WS₂ attractive for numerous applications, and thus proper characterization and easy identification methods of atomically thick MoS₂ and WS₂ are in high demand.⁹

Raman spectroscopy is a powerful nondestructive characterization tool used extensively to study MoS₂ (ref. 9–13) and WS₂.^{1,14,15} Bulk MoS₂ shows two main Raman-active peaks, the in-plane E_{2g}¹ mode at ~382 cm⁻¹ and out-of-plane A_{1g} mode at

~407 cm⁻¹.^{10,16} The former red-shifts while the latter blue-shifts with the number of layers, and thus their frequency difference can be used to identify the number of layers.¹⁰ A similar thickness dependence of frequencies of E_{2g}¹ and A_{1g} modes has been observed for WS₂.¹⁵ However, it remains unclear how Raman intensities and intensity ratio depend on the materials' thickness. Lee *et al.* reported that, for MoS₂ on the SiO₂/Si substrate with a laser wavelength of 514.5 nm, Raman intensities rise up from one to four layers and then decrease for thicker samples, while the peak intensity ratio between E_{2g}¹ and A_{1g} is always higher than 1.¹⁰ Yu *et al.* found that, for MoS₂ on the SiO₂/Si substrate with a laser wavelength of 532 nm, the peak intensity ratio between E_{2g}¹ and A_{1g} remains lower than unity regardless of thickness.¹¹ Reporting on MoS₂ on the same substrate with various laser wavelengths, Li *et al.* found that Raman intensities and intensity ratio of the E_{2g}¹ and A_{1g} peaks vary arbitrarily with thickness.⁹ Similar conflicting results about Raman intensities and intensity ratio have been observed for WS₂.^{1,14} Numerous factors can contribute to this puzzling result: sample quality, substrate,^{10,17} laser polarization,¹⁵ laser wavelength,^{9,14} *etc.* To clarify this issue, we chose free-standing and defect-free MoS₂ and WS₂ up to six-layer-thick, and carried out first-principles density functional theory (DFT) calculations to simulate their Raman spectra and reveal the intrinsic thickness dependence of Raman intensities and intensity ratio of E_{2g}¹ and A_{1g} modes. More importantly, we quantitatively analyzed the laser polarization effect on the intensity ratio to reveal its high sensitivity to laser polarization.

We also studied the Raman spectra of MoS₂/WS₂ heterostructures up to four layers to predict the influence of thickness and stacking order on the details of the spectra. To the best of our knowledge, our work is the first quantitative and systematic *ab initio* study of Raman scattering of MoS₂/WS₂ heterostructures.

Department of Physics, Applied Physics and Astronomy, Rensselaer Polytechnic Institute, Troy, New York 12180, USA. E-mail: meuniv@rpi.edu

† Electronic supplementary information (ESI) available. The thickness dependence of electronic band gaps and dielectric constants of MoS₂ and WS₂ is shown in Fig. S1. Fig. S2 shows *ab initio* Raman spectra of WS₂ and Fig. S3 indicates the laser polarization dependence of the intensity ratio of WS₂. See DOI: 10.1039/c3nr06906k

2 Methodology

As shown in Fig. 1(a) and (c), for one layer, a plane of Mo (or W) atoms is sandwiched covalently between two planes of S atoms in a trigonal prismatic arrangement.⁹ The interaction between layers is dominated by vdW forces. From the top view [Fig. 1(b)], a hexagonal lattice consisting of Mo (or W) and S atoms is clearly seen, similar to graphene and hexagonal boron nitride (h-BN). Its primitive vectors are $\vec{a} = (a, 0, 0)$, $\vec{b} = (-a/2, \sqrt{3}a/2, 0)$, and $\vec{c} = (0, 0, c)$. The symmetry space group of bulk MoS₂ or WS₂ is $P6_3/mmc$ (point group D_{6h}). The space group of MoS₂ or WS₂ with odd number of layers is $P6m2$ (point group D_{3h}), while systems with even number of layers belong to the $P3m1$ space group (point group D_{3d}). All systems exhibit two signature Raman-active modes: E_{2g}^1 and A_{1g} for bulk systems, E' and A'_1 for systems with odd number of layers, and E_g and A_{1g} for systems with even number of layers.^{18,19} For simplicity, the notations of E_{2g}^1 and A_{1g} are used for all systems studied below, which is a common practice in the literature.^{9,10}

The calculations of Raman scattering start with the determination of the equilibrium geometries. Plane-wave DFT calculations were performed using the VASP package²⁰ equipped with the projector augmented-wave (PAW) method²¹ for electron-ion interactions. Local density approximation (LDA) has been shown to yield excellent description of graphite,²² h-BN,²³ graphene/h-BN heterostructures²⁴ and MoS₂.²⁵ Hence, LDA was adopted here for the exchange–correlation interaction

with the energy cutoff set at 500 eV. For bulk MoS₂ and WS₂, both atoms and cell volumes were allowed to relax until the residual forces were below 0.001 eV Å⁻¹. We used a $24 \times 24 \times 4$ k -point sampling in the Monkhorst–Pack scheme.²⁶ The optimized lattice parameters of MoS₂ are $a = 3.13$ and $c = 12.04$ Å (experimental values $a = 3.15$ and $c = 12.30$ Å). For WS₂, $a = 3.13$ and $c = 12.12$ Å (experimental data $a = 3.153$ and $c = 12.323$ Å).²⁵ Obviously, LDA slightly underestimates lattice parameters since it tends to overestimate covalent binding. Single- and few-layer systems, including MoS₂/WS₂ heterostructures, were modeled by a periodic slab geometry using the optimized in-plane lattice constant of the bulk. A vacuum region of 18 Å in the z direction was used to avoid spurious interactions with replicas. For the 2D slab calculations, all atoms were relaxed until the residual forces were below 0.001 eV Å⁻¹ and we used a $24 \times 24 \times 1$ k -point sampling. Since the in-plane lattice mismatch between MoS₂ and WS₂ is very small ($\sim 0.1\%$),^{25,27} the probability of stacking disorders in MoS₂/WS₂ heterostructures is expected to be much smaller than that in graphene/h-BN or MoS₂/MoSe₂ heterostructures.²⁸ Hence, for MoS₂/WS₂ heterostructures, we adapt the in-plane lattice constant of MoS₂ and considered no stacking disordering.

We performed non-resonant first-order Raman calculations using the fully relaxed geometries. The Raman intensity of the j -th phonon mode is given by^{29–31}

$$\frac{d\sigma}{d\Omega} = N_{\text{prim}} \frac{\omega_s^4}{c^4 V_{\text{prim}}} |\mathbf{g}_s \cdot \boldsymbol{\alpha}(j) \cdot \mathbf{g}_i^T|^2 \times \frac{\hbar}{2\omega_j} (n_j + 1), \quad (1)$$

where ω_i and ω_s are the frequencies of the incoming and scattered light, respectively; ω_j is the frequency of the j -th phonon mode of the crystal. Energy conservation imposes $\omega_s = \omega_i \mp \omega_j$, where the minus (plus) sign applies to the Stokes (anti-Stokes) process. In the non-resonant Raman scattering, ω_i only appears in the prefactor ω_s^4 . V_{prim} is the volume of the primitive unit cell, N_{prim} is the number of primitive unit cells in the sample, and c is the speed of light. The Bose factor of the j -th phonon mode is $n_j = (e^{\hbar\omega_j/k_B T} - 1)^{-1}$. \mathbf{g}_i and \mathbf{g}_s are the polarization vectors of the incoming and scattered light.

The Raman susceptibility $\boldsymbol{\alpha}(j)$ is a symmetric (3×3) tensor associated with the j -th phonon mode. It can be computed as^{29,30}

$$\alpha_{\alpha\beta}(j) = V_{\text{prim}} \sum_{\mu=1}^N \sum_{l=1}^3 \frac{\partial \chi_{\alpha\beta}}{\partial r_l(\mu)} \frac{e_l^j(\mu)}{\sqrt{M_\mu}}, \quad (2)$$

where $\chi_{\alpha\beta} = (\varepsilon_{\alpha\beta} - \delta_{\alpha\beta})/4\pi$ is the electric polarizability tensor related to the tensor of dielectric constant $\varepsilon_{\alpha\beta}$, $r_l(\mu)$ is the position of the μ -th atom along the direction l , $\frac{\partial \chi_{\alpha\beta}}{\partial r_l(\mu)}$ is the first derivative of the polarizability tensor (essentially the dielectric constant tensor) over the atomic displacement, $e_l^j(\mu)$ is the displacement of the μ -th atom along the direction l in the j -th phonon mode, and M_μ is the mass of the μ -th atom. Note that e^j and ω_j^2 are the eigenvectors and eigenvalues of the dynamic matrix at the Brillouin zone center, respectively.³⁰

To obtain Raman scattering from eqn (1) and (2), one needs to calculate the dynamic matrix and derivatives of the dielectric constant tensor. The dynamic matrix was calculated using the

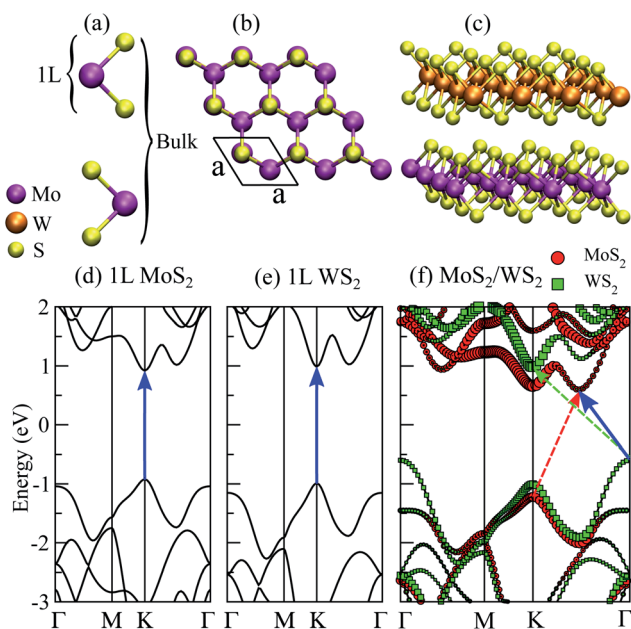


Fig. 1 (a) Side view of MoS₂ bulk and single layer (1L in short). (b) Top view of MoS₂ with the unit cell delineated (analogous for WS₂). (c) Schematic of the heterostructure consisting of 1L MoS₂ and 1L WS₂. Electronic band structures of (d) 1L MoS₂, (e) 1L WS₂ and (f) the heterostructure shown in (c). The solid blue arrows indicate the lowest energy transitions. In (f), red circles (green squares) correspond to projected bands of the MoS₂ (WS₂) layer with the red (green) dashed arrow showing the layer's lowest energy transition. Fermi levels are set at 0 eV.

ab initio direct method,³² implemented in PHONON software.³¹ In the finite difference scheme,^{33,34} the Hellmann–Feynman forces in the supercell were computed by VASP for both positive and negative atomic displacements ($\delta = 0.03$ Å) and used in PHONON to construct the dynamic matrix, whose diagonalization provides phonon frequencies ω_j and normal vectors e^j . The derivatives of the dielectric constant tensor were also calculated by the finite difference approach. For both positive and negative atomic displacements in the single unit cell, the dielectric tensors were computed by VASP using density functional perturbation theory and then imported into PHONON to generate their derivatives. Then the Raman intensity for every phonon mode was obtained for a given laser polarization set-up ($\mathbf{g}_i, \mathbf{g}_s$) and wavelength to finally yield a Raman spectrum after Gaussian broadening. To ensure the accuracy of our calculations, the convergence of both frequency and intensity of the Raman spectrum with respect to the energy cutoff, k -point sampling and vacuum spacing has been carefully studied.

3 Results and discussion

The electronic band structures of monolayer (1L) MoS₂, WS₂ and their bilayer heterostructure are shown in Fig. 1(d)–(f). Both 1L MoS₂ and WS₂ exhibit the well-documented direct band gap.^{6,27} The heterostructure 1L MoS₂/1L WS₂ presents an indirect band gap, as highlighted by the solid blue arrow in Fig. 1(f), consistent with previous theoretical results.³⁵ Similar indirect band gaps are observed for multilayer and bulk MoS₂ and WS₂.^{6,27} To further verify that the direct band gap is not preserved in the individual layer component of the heterostructure, we also computed their projected bands, as shown by red circles and green squares in Fig. 1(f). Clearly, the interlayer coupling between MoS₂ and WS₂ yields indirect band gaps, as indicated by the red and green dashed arrows, just as in multilayer homostructures. Interestingly, in the heterostructure, the lowest energy transition paths [three arrows in Fig. 1(f)] of 1L MoS₂, 1L WS₂ and the whole system are quite different from one another.

The thickness dependence of band gaps of MoS₂ and WS₂ was also studied and is shown in Fig. S1(a) in the ESI.† From 1L to bulk MoS₂ (WS₂), the band gap decreases monotonically from 1.84 (1.98) eV to 0.71 (0.82) eV.²⁷ The noticeable jump of the band gap from 2L and 1L is another sign of the indirect to direct gap transition. For semiconducting MoS₂ and WS₂, non-diagonal elements of the dielectric constant tensor ϵ are zero, and the in-plane dielectric constants $\epsilon_{xx} = \epsilon_{yy}$ due to symmetry. We also computed the thickness dependence of ϵ_{xx} and ϵ_{zz} of MoS₂ and WS₂, as shown in Fig. S1(b).† From 1L to bulk MoS₂, ϵ_{xx} (ϵ_{zz}) monotonically increases from 6.269 (1.471) to 15.452 (7.553), in agreement with previous calculations.²⁵ A similar trend is also observed for WS₂ [lines with triangles in Fig. S1(b)†]. A semiconductor with a smaller band gap generally has larger dielectric constants, and hence the variations of band gaps and dielectric constants with thickness show opposite trends.

Fig. 2(a) shows *ab initio* Raman spectra of free-standing MoS₂ with various thicknesses using a 488 nm laser line. The polarizations of incident and scattered light are set to $\mathbf{g}_i = \mathbf{g}_s = (1, 0, 0)$.

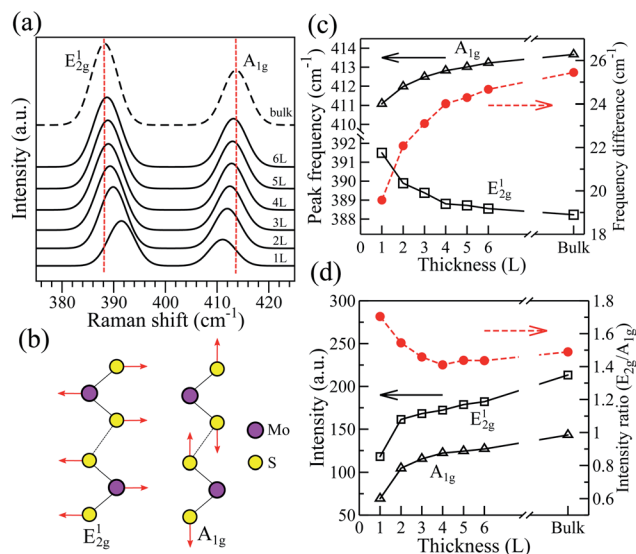


Fig. 2 (a) *Ab initio* Raman spectra of free-standing n -layer (nL) and bulk MoS₂, with laser polarizations $\mathbf{g}_i = \mathbf{g}_s = (1, 0, 0)$ and wavelength 488 nm. (b) Schematic of Raman-active modes E_{2g}¹ and A_{1g} of bulk MoS₂. (c) Frequencies of E_{2g}¹ and A_{1g} (left vertical axis) and their difference (right vertical axis) as a function of layer number. (d) Peak intensities of E_{2g}¹ and A_{1g} (left vertical axis) and their intensity ratio (right vertical axis) as a function of thickness.

The in-plane E_{2g}¹ and out-of-plane A_{1g} Raman modes [Fig. 2(b)] exhibit the strongest signals among all phonon modes. For single-layer MoS₂, the calculated frequencies of E_{2g}¹ and A_{1g} are 391.50 and 411.07 cm⁻¹, respectively. Compared to experimental data ~ 384.3 (E_{2g}¹) and ~ 403 (A_{1g}) cm⁻¹,^{9,10} our LDA calculations systematically overestimate the phonon frequencies by ~ 7 – 8 cm⁻¹, since LDA tends to overbind. Despite the limits of LDA, it successfully reproduces the experimentally observed continuous red-shift of E_{2g}¹ and blue-shift of A_{1g} with increasing thickness,^{9,10} as shown by solid lines in Fig. 2(c). Note that the frequency difference between A_{1g} and E_{2g}¹ is the most effective indicator of the number of layers. The systematic overestimation of frequencies by LDA is expected to be largely canceled out for the frequency difference. Indeed, from 1L to bulk MoS₂ [red dashed line in Fig. 2(c)], the computed frequency difference monotonically increases from 19.57 (experimental value ~ 18.7) cm⁻¹ to 25.44 (experimental value ~ 25.5) cm⁻¹, in excellent agreement with experimental data and confirming the frequency difference as a reliable thickness indicator.¹⁰ As for the mechanisms, the upshift of A_{1g} with increasing thickness is due to the increasing interlayer interactions which enhance the effective restoring forces acting on the atoms, while the more unexpected downshift of E_{2g}¹ with increasing thickness has been attributed to the increasing dielectric screening of the long-range Coulomb forces which reduces the overall restoring force on the atoms.^{10,25} The interlayer coupling and dielectric screening are also vital to explain Raman scattering of the heterostructures discussed below.

Ab initio Raman spectra of free-standing WS₂ are also presented in Fig. S2(a) (ESI†) with the same laser conditions as those used for MoS₂. E_{2g}¹ and A_{1g} modes still exhibit strongest

Raman signals. However, the frequencies of WS_2 E_{2g}^1 mode at any thickness are softened by more than 30 cm^{-1} compared to those of MoS_2 E_{2g}^1 , due to the larger mass of W atoms. For A_{1g} mode in which only sulfur atoms vibrate [Fig. 2(b)], WS_2 has larger frequencies than MoS_2 by more than 9 cm^{-1} . For WS_2 [solid lines in Fig. S2(c)†], our calculations show again the experimentally observed monotonic downshift of E_{2g}^1 and upshift of A_{1g} with increasing thickness.¹⁵ Hence, the frequency difference between A_{1g} and E_{2g}^1 [red dashed line in Fig. S2(c)†] increases monotonically from 60.31 to 64.82 cm^{-1} , in great agreement with experimental data¹⁵ and confirming the frequency difference as a reliable thickness indicator for WS_2 too.

Despite the fact that phonon frequencies have been extensively studied,^{25,36,37} little has been reported regarding a systematic DFT study on Raman intensities of MoS_2 and WS_2 .¹⁸ Here we focus on the evolution of Raman peak intensities with thickness. For free-standing MoS_2 and WS_2 , the peak intensities of E_{2g}^1 and A_{1g} increase significantly from 1L to 2L and then slowly increase until converging to bulk values [solid lines in Fig. 2(d) and S2(d)† respectively]. As discussed above for both MoS_2 and WS_2 , with increasing thickness, the band gap decreases monotonically, the dielectric tensor thus increases, and hence the dielectric tensor's derivatives increase as well. Since Raman intensities are directly related to the dielectric tensor's derivatives [see eqn (1) and (2)], they increase with thickness too, which explains the observed Raman intensities evolution with the layer number. Particularly from 1L to 2L, the dramatic drop of the band gap correlates with the significant increase of the dielectric tensor (Fig. S1 in the ESI†), hence leading to the significant jump of Raman intensities from 1L to 2L [Fig. 2(d) and S2(d)†]. Furthermore, 1L MoS_2 has the highest peak intensity ratio between E_{2g}^1 and A_{1g} (1.71). The intensity ratio drops until 4L and then converges to the bulk value (1.49) [red dashed line in Fig. 2(d)]. Similarly, 1L WS_2 has the highest intensity ratio (2.73), while decreases until 4L and then recovers the bulk value (2.30) [red dashed line in Fig. S2(d)†].

The calculated thickness dependence of peak intensities and intensity ratio is not consistent with experimental observations. In fact, as mentioned in the Introduction, there is a large discrepancy among different experimental works. For MoS_2 on the SiO_2/Si substrate, Lee *et al.* reported that Raman intensities rise up to four layers and then decrease for thicker samples with the peak intensity ratio always higher than 1,¹⁰ Yu *et al.* found that the intensity ratio stays lower than 1 at any thickness,¹¹ and Li *et al.* showed that Raman intensities and intensity ratios vary arbitrarily with thickness.⁹ Similar conflicting results have been observed for WS_2 .^{1,14} The optical interference occurring between incident and scattered laser light, enhanced by the SiO_2/Si substrate,^{10,17} has been considered as a plausible explanation for the observed puzzling behavior of Raman intensities with thickness. The present study on free-standing MoS_2 and WS_2 does not include the substrate and optical interference effects, and might reveal the intrinsic thickness dependence of Raman intensities. It follows that the deviation from experimental observations is expected to some extent. However, since the substrate and optical interference effects are expected to

similarly affect both E_{2g}^1 and A_{1g} modes,^{10,17} the discrepancy between the computed and measured intensity ratios, and particularly the inconsistency between measured intensity ratios by different groups, are perplexing. Here, we postulate that keys to addressing this issue can be found by examining eqn (1): this relationship establishes that the Raman intensity depends on the polarizations of incident and scattered light \mathbf{g}_i and \mathbf{g}_s (*i.e.* laser set-up). To quantify the effect of laser polarizations on intensity ratios, we now carefully explore different laser set-ups.

The in-plane E_{2g}^1 mode is double-degenerated and can vibrate along the x and y directions (denoted as $E_{2g}^1\text{-}x$ and $E_{2g}^1\text{-}y$, respectively). The out-plane A_{1g} mode is non-degenerated. For the $E_{2g}^1\text{-}x$, $E_{2g}^1\text{-}y$ and A_{1g} modes, the Raman tensor $\alpha(j)$ in eqn (2) assumes well-defined forms:

$$\begin{pmatrix} \cdot & a & \cdot \\ a & \cdot & \cdot \\ \cdot & \cdot & \cdot \end{pmatrix}, \begin{pmatrix} a & \cdot & \cdot \\ \cdot & -a & \cdot \\ \cdot & \cdot & \cdot \end{pmatrix} \text{ and } \begin{pmatrix} b & \cdot & \cdot \\ \cdot & b & \cdot \\ \cdot & \cdot & c \end{pmatrix},$$

respectively. In the Raman tensors, a , b and c are major terms while other terms (denoted by “ \cdot ”) are either zero or negligible due to symmetry.^{29,30} From eqn (1), Raman intensity $I \propto |\mathbf{g}_s \cdot \alpha(j) \cdot \mathbf{g}_i|^2$. Hence, when the laser polarizations are set to $\mathbf{g}_i = \mathbf{g}_s = (\cos \theta, 0, \sin \theta)$, the intensity of the A_{1g} mode is

$$I_{A_{1g}} \propto \left| (\cos \theta, 0, \sin \theta) \begin{pmatrix} b & \cdot & \cdot \\ \cdot & b & \cdot \\ \cdot & \cdot & c \end{pmatrix} \begin{pmatrix} \cos \theta \\ 0 \\ \sin \theta \end{pmatrix} \right|^2 \propto |(b-c)\cos^2 \theta + c|^2 \quad (3)$$

and similar matrix operations yield $I_{E_{2g}^1\text{-}x} = 0$, $I_{E_{2g}^1\text{-}y} \propto a^2 \cos^4 \theta$ and $I_{E_{2g}^1} = I_{E_{2g}^1\text{-}x} + I_{E_{2g}^1\text{-}y} \propto a^2 \cos^4 \theta$. Therefore, when the polarization angle θ is varied from 0° to 90° , $I_{E_{2g}^1}$ monotonically decreases from its maximum to zero for both single-layer and bulk MoS_2 [Fig. 3(a) and (c)]. For single-layer MoS_2 , $b > c$, and hence $I_{A_{1g}}$ monotonically reduces from maximum to minimum with θ being varied from 0° to 90° [Fig. 3(a)]. In contrast, $b < c$ for bulk MoS_2 , and thus $I_{A_{1g}}$ monotonically increases from minimum to maximum with θ being varied from 0° to 90° [Fig. 3(c)]. For both single-layer and bulk MoS_2 , with θ being changed from 0° to 90° , the intensity ratio between E_{2g}^1 and A_{1g} monotonically decreases to absolute zero [inset figures in Fig. 3(a) and (c)]. In another laser set-up $\mathbf{g}_i = (1, 0, 0)$ and $\mathbf{g}_s = (\cos \theta, \sin \theta, 0)$, following matrix operations in eqn (3), we have $I_{E_{2g}^1\text{-}x} \propto a^2 \sin^2 \theta$, $I_{E_{2g}^1\text{-}y} \propto a^2 \cos^2 \theta$, $I_{E_{2g}^1} = I_{E_{2g}^1\text{-}x} + I_{E_{2g}^1\text{-}y} \propto a^2$, and $I_{A_{1g}} = b^2 \cos^2 \theta$. $I_{E_{2g}^1}$ is independent of θ and unchanged when θ is varied from 0° to 90° , while $I_{A_{1g}}$ monotonically decreases from its peak to zero for both single-layer and bulk MoS_2 [Fig. 3(b) and (d)], in agreement with recent Raman measurements.^{15,19} Hence, the intensity ratio between E_{2g}^1 and A_{1g} monotonically increases to infinity with θ being varied from 0° to 90° [inset figures in Fig. 3(b) and (d)]. Similar results about polarization-dependent Raman spectra and intensity ratios are found for WS_2 too [see Fig. S3 in the ESI†].

For both MoS_2 and WS_2 , our calculations show that the intensity ratio between E_{2g}^1 and A_{1g} is very sensitive to the laser set-up and can be tuned from 0 to infinity, which could be key to explaining the large discrepancy between measured intensity

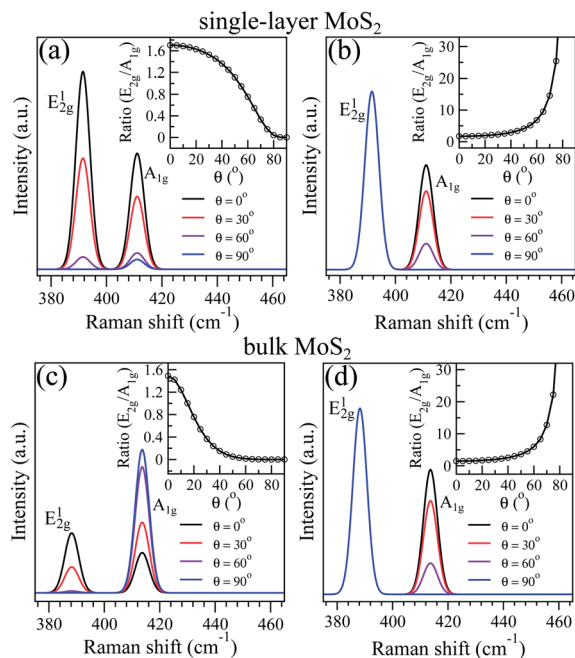


Fig. 3 Raman spectra of (a) single-layer and (c) bulk MoS₂ with laser polarizations $\mathbf{g}_i = \mathbf{g}_s = (\cos \theta, 0, \sin \theta)$. Raman spectra of (b) single-layer and (d) bulk MoS₂ with laser polarizations $\mathbf{g}_i = (1, 0, 0)$ and $\mathbf{g}_s = (\cos \theta, \sin \theta, 0)$. In (a) and (c), some of Raman spectra are scaled for comparison purpose. The inset figures show the intensity ratio between E_{2g}^1 and A_{1g} as a function of θ .

ratios by different groups. Even in the same experimental work using the same laser set-up, samples with different layers could have different orientations, equivalent to different polarization set-ups for the samples with the same orientation, which might lead to the arbitrary evolution of the intensity ratio with thickness as observed by Li *et al.*, for instance.⁹ Note that in the non-resonant first-order Raman scattering considered in this work, the incident laser frequency affects both Raman modes identically, exerting essentially no influence on the intensity ratio (more details in the ESI†).

After the detailed analysis of Raman spectra of MoS₂ and WS₂, we now turn our attention to Raman scattering of MoS₂/WS₂ heterostructures.³⁸ For vdW-bonded layered systems such as graphite, h-BN and MX₂, layers can be micromechanically separated and reassembled to form heterostructures, which can show combined functionality of the individual layers, can lead to new emergent properties and are thus very desirable.^{2,16} Here, we carefully examined first-principles Raman scattering of MoS₂/WS₂ heterostructures (Fig. 4) to establish that their Raman spectra can be used to identify the stoichiometry and stacking patterns. For simplicity, a MoS₂ (WS₂) layer is denoted as Mo (W) in Fig. 4. Hence, MoW stands for the heterostructure 1L MoS₂/1L WS₂, MoMoW for 2L MoS₂/1L WS₂, MoMoWW for 2L MoS₂/2L WS₂, etc. From 2L to 4L heterostructures, Raman spectra of all non-equivalent stacking patterns are examined as shown in Fig. 4(b). For MoW, its Raman spectrum shows features of both MoS₂ and WS₂. Compared to the Raman spectra of Mo and W in Fig. 4(b), the E_{2g}^1 peak of MoW corresponding to Mo (E_{2g}^1 -Mo) is clearly red-shifted, and the E_{2g}^1 peak of MoW

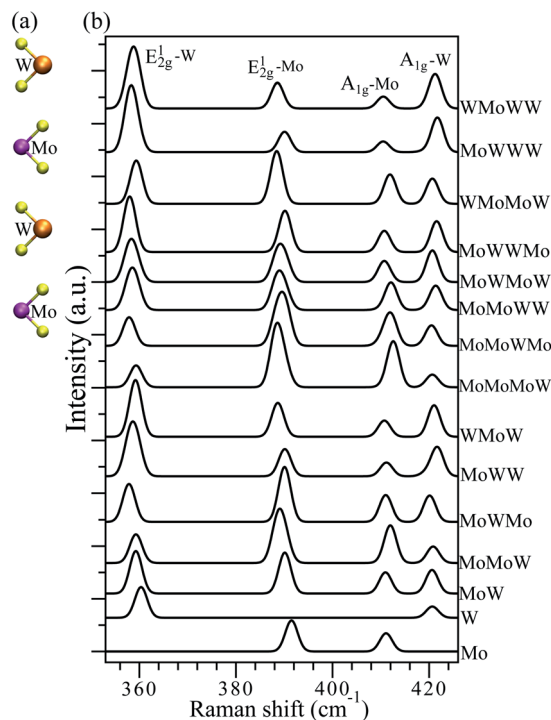


Fig. 4 Raman spectra of MoS₂/WS₂ heterostructures. (a) Schematic of a heterostructure with stacking pattern MoW, where a MoS₂ (WS₂) layer is denoted as Mo (W) for simplicity. (b) *Ab initio* Raman spectra of various MoS₂/WS₂ heterostructures, with laser polarizations $\mathbf{g}_i = \mathbf{g}_s = (1, 0, 0)$ and wavelength 488 nm. The Raman spectra of single-layer MoS₂ (Mo) and WS₂ (W) are also reproduced here for comparison.

corresponding to W (E_{2g}^1 -W) is red-shifted too, while A_{1g} -Mo and A_{1g} -W peaks of MoW are barely shifted. As mentioned above, the red-shift of E_{2g}^1 -Mo of MoW is ascribed to increased dielectric screening to the Mo layer in the presence of the W layer, and *vice versa*.²⁵ For MoW, the frequency difference between A_{1g} and E_{2g}^1 of MoS₂ (WS₂) in the heterostructure, denoted as $\Delta\omega$ -Mo ($\Delta\omega$ -W), is 20.83 (61.33) cm⁻¹, according to Table 2. From Table 1, $\Delta\omega$ are 19.58 and 22.08 cm⁻¹ for Mo and MoMo, respectively. $\Delta\omega$ are 60.31 and 62.18 cm⁻¹ for W and WW, respectively. Obviously, $\Delta\omega$ -Mo of MoW ranges between $\Delta\omega$ of Mo and MoMo, and its $\Delta\omega$ -W is between $\Delta\omega$ of W and WW. In other words, for MoW, the addition of the W (Mo) layer increases $\Delta\omega$ of the Mo (W) layer but not as significantly as the addition of another Mo (W) layer. Free-standing MoW and WMo are equivalent and no difference between their Raman spectra is

Table 1 $\Delta\omega$ indicates the frequency difference between A_{1g} and E_{2g}^1 modes for pure MoS₂ and WS₂. Mo (W) means 1L MoS₂ (WS₂), MoMo (WW) means 2L MoS₂ (WS₂), etc.

Stacking	Mo	MoMo	MoMoMo	MoMoMoMo
$\Delta\omega$ (cm ⁻¹)	19.58	22.08	23.10	24.01
Stacking	W	WW	WWW	WWWW
$\Delta\omega$ (cm ⁻¹)	60.31	62.18	63.13	63.50

expected. In contrast, when they are supported on a substrate, the environmental change might lead to some variations between their Raman spectra. However, the differences are expected to be small since the substrate only weakly interacts with the heterostructures.

For 3L heterostructure MoMoW in Fig. 4(b), compared to MoW, its E_{2g}^1 -Mo peak is red-shifted due to the increased dielectric screening to Mo while the A_{1g} -Mo peak is blue-shifted due to the increased interlayer interaction with Mo, while its E_{2g}^1 -W and A_{1g} -W peaks are hardly shifted since the close environment of W does not change appreciably. Therefore, $\Delta\omega$ -Mo of MoMoW is increased to 22.90 cm^{-1} [Table 2], between $\Delta\omega$ of MoMo and MoMoMo [Table 1]. Similarly, for MoWW in Fig. 4(b), compared to MoW, its E_{2g}^1 -W peak is red-shifted due to the increased dielectric screening to W while the A_{1g} -W peak is blue-shifted due to the increased interlayer interaction with W, while its E_{2g}^1 -Mo and A_{1g} -Mo peaks are hardly shifted since the environment of Mo is hardly modified. Hence, $\Delta\omega$ -W of MoWW is increased to 62.97 cm^{-1} [Table 2], between $\Delta\omega$ of WW and WWW [Table 1]. Similarly, for MoMoW (MoWW), the addition of the W (Mo) layer increases $\Delta\omega$ of the Mo (W) layers but not as significantly as the addition of another Mo (W) layer. Another interesting phenomenon is that $\Delta\omega$ -Mo and $\Delta\omega$ -W for the heterostructures are also sensitive to stacking patterns. For MoWMo in Fig. 4(b), compared to MoMoW, the dielectric screening to W is increased since the W layer is now sandwiched between two Mo layers, while the dielectric screening to Mo is decreased. It follows that the E_{2g}^1 -W peak of MoWMo is clearly red-shifted while its E_{2g}^1 -Mo peak is blue-shifted. Therefore, in spite of the same stoichiometry of Mo : W, from MoMoW to MoWMo in Table 2, $\Delta\omega$ -W increases from 61.53 to 62.26 cm^{-1} , while $\Delta\omega$ -Mo decreases from 22.90 to 20.94 cm^{-1} . Conversely, from MoWW to WMoW in Fig. 4(b), the dielectric screening to Mo (W) is increased (decreased) and thus the E_{2g}^1 -Mo (E_{2g}^1 -W) peak is red-shifted (blue-shifted). Hence in Table 2, in spite of the same stoichiometry, from MoWW to WMoW, $\Delta\omega$ -Mo increases from 21.04 to 22.06 cm^{-1} , while $\Delta\omega$ -W decreases from 62.97 to 61.82 cm^{-1} . For 4L heterostructures, similar trends can

be observed in Fig. 4 and Tables 1 and 2. In summary, the frequency difference $\Delta\omega$ has been established as a reliable thickness indicator for pure MoS_2 and WS_2 . For heterostructures, the distinctive dependence of $\Delta\omega$ -Mo and $\Delta\omega$ -W on both stoichiometry and stacking patterns revealed in Table 2 can be employed to determine both stoichiometry and stacking patterns.

Turning to intensity ratios, we defined $r\text{-}E_{2g}^1$ ($r\text{-}A_{1g}$) as the intensity ratio between MoS_2 and WS_2 E_{2g}^1 (A_{1g}) in the heterostructures. They are also found to exhibit unique dependence on both stoichiometry and stacking patterns. With a laser set-up $\mathbf{g}_i = \mathbf{g}_s = (1, 0, 0)$ in Table 2, $r\text{-}E_{2g}^1$ and $r\text{-}A_{1g}$ of MoW are 0.96 and 0.90 respectively, close to the stoichiometry of Mo : W (1 : 1). For MoMoW, $r\text{-}E_{2g}^1$ ($r\text{-}A_{1g}$) grows to 1.89 (2.29), around the stoichiometry of Mo : W (2 : 1). For MoWW, $r\text{-}E_{2g}^1$ ($r\text{-}A_{1g}$) drops to 0.50 (0.46), around the stoichiometry of Mo : W (1 : 2). For MoMoMoW, $r\text{-}E_{2g}^1$ ($r\text{-}A_{1g}$) is 2.99 (3.63), around the stoichiometry of Mo : W (3 : 1). For MoWWWW, $r\text{-}E_{2g}^1$ ($r\text{-}A_{1g}$) is 0.30 (0.31), close to the stoichiometry of Mo : W (1 : 3). Hence, $r\text{-}E_{2g}^1$ and $r\text{-}A_{1g}$ are an indicator of the stoichiometry of heterostructures. Furthermore, $r\text{-}E_{2g}^1$ and $r\text{-}A_{1g}$ are sensitive to the stacking order as well. Based on the same argument developed for pure MoS_2 and WS_2 above, from MoMoW to MoWMo, the dielectric screening to W (Mo) is increased (decreased), the localized band gap of W (Mo) is decreased (increased), the effective dielectric constant tensor of W (Mo) is slightly increased (decreased), and thus Raman intensities of W (Mo) should be increased (decreased). Indeed, from MoMoW to MoWMo in Fig. 4(b), Raman intensities of E_{2g}^1 -W and A_{1g} -W are increased while those of E_{2g}^1 -Mo and A_{1g} -Mo are slightly decreased, and hence $r\text{-}E_{2g}^1$ ($r\text{-}A_{1g}$) is decreased to 1.45 (1.02) in Table 2. Similarly, from MoMoMoW to MoMoWMo, the dielectric screening to W (Mo) is increased (decreased), Raman intensities of W (Mo) are increased (decreased) [Fig. 4(b)], and hence $r\text{-}E_{2g}^1$ and $r\text{-}A_{1g}$ are decreased [Table 2]. In contrast, from MoWW to WMoW, the dielectric screening to Mo (W) is increased (decreased), eventually leading to the increase of $r\text{-}E_{2g}^1$ and $r\text{-}A_{1g}$ in Table 2. From MoWWWW to WMoWW, the dielectric screening to Mo (W) is again increased (decreased), and thus $r\text{-}E_{2g}^1$ and $r\text{-}A_{1g}$ are increased.

Table 2 $\Delta\omega$ -Mo ($\Delta\omega$ -W) is the frequency difference between A_{1g} and E_{2g}^1 modes of MoS_2 (WS_2) in the MoS_2/WS_2 heterostructures, and $r\text{-}E_{2g}^1$ ($r\text{-}A_{1g}$) means the intensity ratio between MoS_2 and WS_2 E_{2g}^1 (A_{1g})

Stacking	$\Delta\omega$ -Mo (cm^{-1})	$\Delta\omega$ -W (cm^{-1})	$r\text{-}E_{2g}^1$	$r\text{-}A_{1g}$
MoW	20.83	61.33	0.96	0.90
MoMoW	22.90	61.53	1.89	2.29
MoWMo	20.94	62.26	1.45	1.02
MoWW	21.04	62.97	0.50	0.46
WMoW	22.06	61.82	0.60	0.51
MoMoMoW	23.98	61.34	2.99	3.63
MoMoWMo	22.37	62.61	1.89	1.64
MoMoWW	23.07	62.80	0.93	1.13
MoWMoW	21.47	62.31	0.89	0.67
MoWWMo	20.58	63.55	0.74	0.70
WMoMoW	23.45	61.31	1.22	1.16
MoWWWW	20.41	63.38	0.30	0.31
WMoWW	21.91	62.45	0.41	0.35

4 Conclusion

We have performed a comprehensive first-principles study of Raman scattering of MoS_2 , WS_2 and their heterostructures. For MoS_2 and WS_2 , our calculations successfully reproduce the experimentally observed continuous downshift of E_{2g}^1 mode and upshift of A_{1g} mode with increasing thickness. The increasing dielectric screening (interlayer coupling) is found to be responsible for the downshift of E_{2g}^1 (upshift of A_{1g}) with increasing thickness. In MoS_2/WS_2 heterostructures, the same dielectric screening and interlayer coupling effects lead to a distinctive dependence of $\Delta\omega$ -Mo and $\Delta\omega$ -W on both the stoichiometry and stacking patterns.

For free-standing MoS_2 and WS_2 , we also report the intrinsic thickness dependence of Raman intensities and intensity ratio of E_{2g}^1 and A_{1g} modes. More importantly, both Raman intensities and intensity ratio are found to be very sensitive to the laser

set-up, and we demonstrate how the intensity ratio can be essentially tuned from zero to infinity by adjusting laser polarizations, which might explain the inconsistency in measured intensity ratios. For the heterostructures, $r\text{-E}_{2g}^1$ and $r\text{-A}_{1g}$ show a distinctive dependence on both the stoichiometry and stacking patterns as well, in which the dielectric screening plays a key role. The combination of $\Delta\omega\text{-Mo}$, $\Delta\omega\text{-W}$, $r\text{-E}_{2g}^1$ and $r\text{-A}_{1g}$ in Table 2 is expected to serve as a guideline for the experimental characterization of the heterostructures.

Note that very recently, surface effects have been proposed by Luo *et al.* as an alternative mechanism to explain the anomalous downshift of E_{2g}^1 with increasing thickness.¹⁸ For MoS_2 , surface effects refer to the larger Mo–S force constants at the surface of thin film MoS_2 , which results from a loss of neighbors in adjacent MoS_2 layers. With increasing thickness, there are more neighbors from adjacent layers and hence surface force constants decrease, resulting in the frequency decrease of E_{2g}^1 . It is still under debate whether dielectric screening²⁵ or surface effects¹⁸ are responsible for the downshift of E_{2g}^1 with increasing thickness. Nevertheless, surface effects can be also applied to explain the dependence of the $\text{E}_{2g}^1\text{-Mo}$ and $\text{E}_{2g}^1\text{-W}$ peaks on both stoichiometry and stacking patterns in the heterostructures. For example, from MoMoW to MoWMo in Fig. 4(b), the surface force constants of W are decreased since the W layer is now sandwiched between two Mo layers (more neighbors), while the surface force constants of Mo are increased (less neighbors). It follows that the $\text{E}_{2g}^1\text{-W}$ peak of MoWMo is clearly red-shifted while its $\text{E}_{2g}^1\text{-Mo}$ peak is blue-shifted. In short, the conclusions made for heterostructures hold no matter which mechanism (dielectric screening or surface effects) is predominant.

Acknowledgements

The authors are supported by New York State under NYSTAR contract C080117 and by the US Army Research Laboratory through the Multiscale Modeling of Electronic Materials Collaborative Research Alliance. All calculations were performed in the Center for Computational Innovation at Rensselaer Polytechnic Institute.

References

- 1 H. Zeng, G.-B. Liu, J. Dai, Y. Yan, B. Zhu, R. He, L. Xie, S. Xu, X. Chen, W. Yao and X. Cui, *Sci. Rep.*, 2013, **3**, 1608.
- 2 S. Z. Butler, S. M. Hollen, L. Cao, Y. Cui, J. A. Gupta, H. R. Gutierrez, T. F. Heinz, S. S. Hong, J. Huang, A. F. Ismach, E. Johnston-Halperin, M. Kuno, V. V. Plashnitsa, R. D. Robinson, R. S. Ruoff, S. Salahuddin, J. Shan, L. Shi, M. G. Spencer, M. Terrones, W. Windl and J. E. Goldberger, *ACS Nano*, 2013, **7**, 2898–2926.
- 3 K. Novoselov, A. Geim, S. Morozov, D. Jiang, Y. Zhang, S. Dubonos, I. Grigorieva and A. Firsov, *Science*, 2004, **306**, 666–669.
- 4 B. Radisavljevic, A. Radenovic, J. Brivio, V. Giacometti and A. Kis, *Nat. Nanotechnol.*, 2011, **6**, 147–150.
- 5 W. Ho, J. C. Yu, J. Lin, J. Yu and P. Li, *Langmuir*, 2004, **20**, 5865–5869.
- 6 A. Splendiani, L. Sun, Y. Zhang, T. Li, J. Kim, C.-Y. Chim, G. Galli and F. Wang, *Nano Lett.*, 2010, **10**, 1271–1275.
- 7 K. F. Mak, C. Lee, J. Hone, J. Shan and T. F. Heinz, *Phys. Rev. Lett.*, 2010, **105**, 136805.
- 8 H. R. Gutierrez, N. Perea-Lopez, A. L. Elias, A. Berkdemir, B. Wang, R. Lv, F. López-Urías, V. H. Crespi, H. Terrones and M. Terrones, *Nano Lett.*, 2012, **13**, 3447.
- 9 H. Li, Q. Zhang, C. C. R. Yap, B. K. Tay, T. H. T. Edwin, A. Olivier and D. Baillargeat, *Adv. Funct. Mater.*, 2012, **22**, 1385–1390.
- 10 C. Lee, H. Yan, L. E. Brus, T. F. Heinz, J. Hone and S. Ryu, *ACS Nano*, 2010, **4**, 2695–2700.
- 11 Y. Yu, C. Li, Y. Liu, L. Su, Y. Zhang and L. Cao, *Sci. Rep.*, 2013, **3**, 1866.
- 12 Y.-H. Lee, L. Yu, H. Wang, W. Fang, X. Ling, Y. Shi, C.-T. Lin, J.-K. Huang, M.-T. Chang, C.-S. Chang, M. Dresselhaus, T. Palacios, L.-J. Li and J. Kong, *Nano Lett.*, 2013, **13**, 1852–1857.
- 13 N. A. Lanzillo, A. Glen Birdwell, M. Amani, F. J. Crowne, P. B. Shah, S. Najmaei, Z. Liu, P. M. Ajayan, J. Lou, M. Dubey, S. K. Nayak and T. P. O'Regan, *Appl. Phys. Lett.*, 2013, **103**, 093102.
- 14 A. Berkdemir, H. R. Gutiérrez, A. R. Botello-Méndez, N. Perea-López, A. L. Elias, C.-I. Chia, B. Wang, V. H. Crespi, F. López-Urías, J.-C. Charlier, H. Terrones and M. Terrones, *Sci. Rep.*, 2013, **3**, 1755.
- 15 W. Zhao, Z. Ghorannevis, K. K. Amara, J. R. Pang, M. Toh, X. Zhang, C. Kloc, P. H. Tan and G. Eda, *Nanoscale*, 2013, **5**, 9677.
- 16 A. C. Ferrari and D. M. Basko, *Nat. Nanotechnol.*, 2013, **8**, 235–246.
- 17 S.-L. Li, H. Miyazaki, H. Song, H. Kuramochi, S. Nakaharai and K. Tsukagoshi, *ACS Nano*, 2012, **6**, 7381–7388.
- 18 X. Luo, Y. Zhao, J. Zhang, Q. Xiong and S. Y. Quek, *Phys. Rev. B: Condens. Matter Mater. Phys.*, 2013, **88**, 075320.
- 19 X. Luo, Y. Zhao, J. Zhang, M. Toh, C. Kloc, Q. Xiong and S. Y. Quek, *Phys. Rev. B: Condens. Matter Mater. Phys.*, 2013, **88**, 195313.
- 20 G. Kresse and J. Furthmüller, *Comput. Mater. Sci.*, 1996, **6**, 15–50.
- 21 G. Kresse and D. Joubert, *Phys. Rev. B: Condens. Matter Mater. Phys.*, 1999, **59**, 1758.
- 22 G. Kresse, J. Furthmüller and J. Hafner, *Europhys. Lett.*, 1995, **32**, 729.
- 23 G. Kern, G. Kresse and J. Hafner, *Phys. Rev. B: Condens. Matter Mater. Phys.*, 1999, **59**, 8551.
- 24 G. Giovannetti, P. Khomyakov, G. Brocks, P. Kelly and J. van den Brink, *Phys. Rev. B: Condens. Matter Mater. Phys.*, 2007, **76**, 073103.
- 25 A. Molina-Sánchez and L. Wirtz, *Phys. Rev. B: Condens. Matter Mater. Phys.*, 2011, **84**, 155413.
- 26 H. J. Monkhorst and J. D. Pack, *Phys. Rev. B: Condens. Matter Mater. Phys.*, 1976, **13**, 5188–5192.
- 27 W. S. Yun, S. Han, S. C. Hong, I. G. Kim and J. Lee, *Phys. Rev. B: Condens. Matter Mater. Phys.*, 2012, **85**, 033305.

- 28 J. Kang, J. Li, S.-S. Li, J.-B. Xia and L.-W. Wang, *Nano Lett.*, 2013, **13**, 5485–5490.
- 29 P. Umari, A. Pasquarello and A. Dal Corso, *Phys. Rev. B: Condens. Matter Mater. Phys.*, 2001, **63**, 094305.
- 30 M. Ceriotti, F. Pietrucci and M. Bernasconi, *Phys. Rev. B: Condens. Matter Mater. Phys.*, 2006, **73**, 104304.
- 31 K. Parlinski, *Software PHONON*, Poland, 2010.
- 32 K. Parlinski, Z. Li and Y. Kawazoe, *Phys. Rev. Lett.*, 1997, **78**, 4063.
- 33 L. Liang, E. Cruz-Silva, E. Girão and V. Meunier, *Phys. Rev. B: Condens. Matter Mater. Phys.*, 2012, **86**, 115438.
- 34 L. Liang and V. Meunier, *Appl. Phys. Lett.*, 2013, **102**, 143101.
- 35 H. Terrones, F. López-Uriás and M. Terrones, *Sci. Rep.*, 2013, **3**, 1549.
- 36 C. Ataca, M. Topsakal, E. Akturk and S. Ciraci, *J. Phys. Chem. C*, 2011, **115**, 16354.
- 37 C. Rice, R. Young, R. Zan, U. Bangert, D. Wolverson, T. Georgiou, R. Jalil and K. Novoselov, *Phys. Rev. B: Condens. Matter Mater. Phys.*, 2013, **87**, 081307.
- 38 N. Lu, H. Guo, L. Lei, J. Dai, L. Wang, W.-N. Mei, X. Wu and X. C. Zeng, *Nanoscale*, 2014, 2879.